RSC Advances

PAPER

View Article Online
View Journal | View Issue

Cite this: *RSC Adv.*, 2025, **15**, 33410

Synthesis, spectroscopic properties, structural characterization, and computational studies of a new non-centrosymmetric hybrid compound: bis-cyanato-*N* chromium(III) *meso*-arylporphyrin complex

Mondher Dhifet, *[ab] Nabil Benzerroug,[c] Tahani M. Almutairi,*[d] Khadra B. Alomari,[e] Nikolay Tumanov [f] and Noureddine Issaoui [gh]

In this work, we report the synthesis and spectroscopic properties of a hexa-coordinated chromium(III) porphyrin complex, namely, bis(cyanato-*N*)[*meso*-tetraphenylporphyrinato]chromate(III) (cryptand-222) sodium chloroform monosolvate with the formula $[Na(2,2,2\text{-crypt})][Cr^{III}(TPP)(NCO)_2]\cdot 0.406CHCl_3$ (**I**). Complex **I** was characterized in solution by UV/vis and IR spectroscopies. The structural determination of compound **I** was performed by single-crystal X-ray diffraction and Hirshfeld surface area calculations. This compound crystallized in the triclinic system with the non-centrosymmetric space group *P*1. The average distance between the central Cr(III) ion and the nitrogen atoms in the equatorial position is 2.039(3) Å, while the Cr^{III}–N (axial ligand) distances from the bis-cyanate ligand are 2.012(3) Å and 2.016(4) Å. Crystal packing cohesion was stabilized by unconventional intramolecular C–H···O and C–H···Cl hydrogen bonds. In addition, we conducted a theoretical investigation of several key physical properties to provide a comprehensive understanding of the electron charge transfer mechanisms of the chromium(III) porphyrin complex using density functional theory (DFT) at the B3LYP-D3/LanL2DZ level. This includes the analysis of frontier molecular orbitals (FMOs) and associated reactivity descriptors; molecular electrostatic potential (MEP) assessment; non-covalent interaction (NCI) analysis through reduced density gradient (RDG) surfaces and bond critical points (BCPs); as well as electron localization function (ELF), localized orbital locator (LOL), and Hirshfeld surface analyses.

Received 19th June 2025
Accepted 19th August 2025

DOI: 10.1039/d5ra04378f

rsc.li/rsc-advances

1. Introduction

The chemistry of synthetic porphyrins and materials based on them is an important area of modern fundamental science as it is associated with the solution of many urgent problems in the development of modern society. Finding solutions to the fundamental problems related to this class of compounds and their practical applications is directly dependent on the optimization of porphyrin synthesis methods and the possibility of chemical modification.[1] This class of compounds has gained interest, first of all, because of their wide participation in various vital biological processes observed in natural systems such as chlorophylls, hemoglobin, myoglobin, cytochromes P460, catalases and peroxidases.[2] Currently, the field of application of porphyrins and metalloporphyrins is very broad and continues to expand. In recent years, some porphyrin compounds have been used as biosensors, and new research aims to use these compounds in the nanomaterial industry.[3–5]

Chromium(III) porphyrin complexes are currently present in many applications such as chemistry, biology, medicine, electronics, and physics. Today, porphyrins are employed in a wide array of fields, including catalysis,[6] photovoltaics,[7] sensing,[8] photodynamic therapy (PDT),[9] supramolecular chemistry,[10] photocatalysis,[11] semiconductors[12,13] and optoelectronic systems.[14] Years of study of these compounds have shown that structural modification of the porphyrin macrocycle allows for

[a]*Laboratory of Physical Chemistry of Materials (LR01ES19), Faculty of Sciences of Monastir, Avenue of the Environment, 5019 Monastir, Tunisia. E-mail: mondherdhifet_2005@yahoo.fr*

[b]*Faculty of Sciences of Gafsa, University of Gafsa, Sidi Ahmed Zarrouk, 2112 Gafsa, Tunisia*

[c]*Laboratory of Micro-Optoelectronics and Nanostructures (LR99ES29), Faculty of Sciences of Monastir, University of Monastir, Avenue of the Environment, Monastir 5019, Tunisia*

[d]*Department of Chemistry, College of Science King Saud University, Riyadh 11451, Saudi Arabia. E-mail: Talmutari1@ksu.edu.sa*

[e]*Jazan University, Department of Physical Sciences, Chemistry Division, P. O. Box 114, 45142, Jazan, Saudi Arabia*

[f]*University of Namur, Rue de Bruxelles 61, 5000 Namur, Belgium*

[g]*University of Monastir, Laboratory of Quantum and Statistical Physics LR18ES18, Faculty of Sciences of Monastir, Monastir, 5079, Tunisia*

[h]*Higher Institute of Computer Sciences and Mathematics of Monastir, University of Monastir, Monastir 5000, Tunisia*

broad variations in the physicochemical properties of porphyrins and metalloporphyrins and, in many cases, determines their effectiveness. Among synthetic porphyrins, *meso*-substituted derivatives are the most studied as they possess tremendous potential for structural transformation. It has been shown that their properties can be easily modulated by the nature of the substituents attached to the tetrapyrrolic macrocycle and by the choice of the metallo-complex, which has the ability to complex almost any metal ion in the periodic table, for example, zinc(II) and magnesium(II) complexes with different axial ligands.[15] Furthermore, the central metal of these metalloporphyrins can coordinate axial ligands of various types. Axial coordination is a process that profoundly alters the spectroscopic, photophysical, and structural properties of metalloporphyrins.

In order to better understand the electrochemical and spectroscopic properties of chromium porphyrins, we synthesized a new hexacoordinated coordination compound, titled bis(cyanato-*N*)[*meso*-tetraphenylporphyrinato]chromate(III) (cryptand-222) sodium chloroform monosolvate. This compound and its precursors were characterized by various spectral methods (UV-visible and IR). Structural determination was performed by single-crystal X-ray diffraction, complemented by a Hirshfeld surface study of complex **I**. To strengthen the overall coherence of this study, we performed a comprehensive theoretical analysis of the investigated complex through advanced computational methods, aiming to gain deeper insights into its structural and electronic behavior.

2. Experimental details

2.1. Materials and methods

All solvents and reagents were obtained from commercial suppliers and used without further purification unless otherwise specified. Solvents employed in the synthesis were purified according to established procedures reported in the literature.[16] All reactions were conducted under ambient conditions.

Fourier transform infrared (FT-IR) spectra were recorded using a PerkinElmer Spectrum Two spectrometer.

Electronic absorption spectra were recorded at room temperature using a SHIMADZU UV-2401 spectrometer.

Elemental analyses were performed using a Flash EA 1112 Series analyzer (Thermo Electron) fitted with a Prepack column 2 m (PTFE) and an MX5 microbalance (Mettler Toledo). Hirshfeld surfaces (HSs) and 2D fingerprint plots (FPs) were generated using CrystalExplorer 17.5,[17,18] based on the data obtained from X-ray diffraction analysis. The d_{norm} function represents a normalized ratio that incorporates the distances from a designated surface point to the closest internal (d_i) and external (d_e) atoms, relative to the van der Waals radii associated with the respective atoms.[17,19]

2.2. X-ray characterization

A dark purple, block-shaped single crystal of complex **I**, measuring 0.22 × 0.12 × 0.11 mm^3, was selected for X-ray diffraction analysis. Data collection was performed at 100 K using an APEX5 v2023.9-2 Bruker D8 Venture diffractometer with Ag Kα radiation (wavelength 0.56086 Å). Reflection data were scaled and corrected for absorption using the numerical program.[20] The structure was solved by direct methods using SIR (2004)[21] and refined by full-matrix least-squares procedures on F^2 using the SHELXL (2014) software.[22] During the refinement of the structure complex **I**, there were some disorder problems encountered:

(i) The oxygen O2 and the carbon C46 of the one axial ligand NCO^- of one $[Cr^{III}(TPP)(NCO)_2]^-$ ion complex are disordered in two positions: C46A-O2A/C46B-O2B with major position occupancies of 0.56873(1).

(ii) The two counterions $[Na1(2,2,2\text{-crypt})]^+$ and $[Na2(2,2,2\text{-crypt})]^+$ are disordered over two orientations with refined occupancy coefficients converged to 0.56873(1) (for the first $[Na1A(2,2,2\text{-crypt})]^+$) and 0.71542(1) (for the second $[Na2A(2,2,2\text{-crypt})]^+$).

(iii) The chloride and the carbon atoms of chloroform solvent are disordered in two positions: C129-Cl1A-Cl2A-Cl3A/C130-Cl1B-Cl2B-Cl3B with major position occupancies of 0.75574(2). Hydrogen atoms were positioned using calculated coordinates and refined as riding on their respective parent atoms. Geometry-related analyses were performed using the PLATON program,[23] and molecular and packing representations were created using MERCURY.[24] The crystallographic and

Table 1 Crystallographic data for $[Na(2,2,2\text{-crypt})][Cr^{III}(TPP)(NCO)_2]\cdot 0.406CHCl_3$ (**I**)

Formula	$C_{64.41}H_{64.41}Cl_{1.22}CrN_8NaO_8$
Formula weight, M	1196.69
Crystal system	Triclinic
Space group	$P\bar{1}$
a (Å)	12.9467(12)
b (Å)	16.0849(15)
c (Å)	17.0355(16)
α (°)	63.553(3)
β (°)	69.614(3)
γ (°)	71.150(3)
V (Å^3)	2917.1(5)
Z	2
$\rho_{calc.}$ (g cm^{-3})	1.362
μ (mm^{-1})	0.176
F (000)	1253
Crystal size (mm^3)	0.22 × 0.12 × 0.11
Crystal color	Purple
Crystal shape	Block
T (K)	150
$\theta_{min} - \theta_{max}$ (°)	2.039–21.552
Limiting indices	$-16 \le h \le 16$, $-20 \le k \le 20$, $-22 \le l \le 22$
R (int)	0.0775
R (sigma)	0.0454
Measured reflections	23 480
Reflections independent	27 027
Parameters/restraints	2053/2760
S [goodness of fit]	1.034
R_1[a], wR_2[b] [$F_o > 4\sigma(F_o)$]	$R1 = 0.0439$, $wR_2 = 0.1125$
wR_2 [all data]	$R1 = 0.0530$, $wR_2 = 0.1187$
Min./max. res. (eÅ^{-3})	0.369/−0.388
CCDC	2414564

[a] $R_1 = \sum||F_o| - |F_c||/\sum|F_o|$. [b] $wR_2 = \{\sum[w(|F_o|^2 - |F_c|^2)^2]/[w(|F_o|^2)^2]\}^{1/2}$.

refinement characteristics of complex **I** are summarized in Table 1.

2.3. Synthesis and crystallization of [Na(2,2,2-crypt)][Cr^{III}(TPP)$(NCO)_2$]·0.406$CHCl_3$

The ligand H_2TPP and the complex [Cr^{III}(TPP)Cl] were synthesized according to previously reported procedures.[25,26] The structure of the synthesized compound was confirmed using advanced analytical techniques prior to its use in subsequent steps. A mixture of sodium cyanate (50 mg, 0.769 mmol) and cryptand-222 (40 mg, 0.106 mmol) was stirred together in chloroform (30 mL) at room temperature for 3 h. Then a solution of [Cr^{III}(TPP)Cl] (40 mg, 0.057 mmol) in chloroform (25 mL) was added, and the reaction mixture was stirred overnight, during which the solution's color changed from purple to green-blue. Crystals of [Na(2,2,2-crypt)][Cr^{III}(TPP)$(NCO)_2$] (**I**) were obtained in approximately 90% yield *via* slow diffusion of *n*-hexane within the chloroform solution.

Elemental analysis calcd (%) for $C_{64.41}H_{64.41}Cl_{1.22}CrN_8NaO_8$ (1196.694 g mol^{-1}): C 64.64, H 5.42, N 9.36; found: C 64.93, H 5.46, N 9.46;

UV-visible: [λ_{max} (nm) in $CHCl_3$, (log ε)]: 403 (4.25), 454 (5.13), 534 (2.56), 583 (3.41), 618 (3.72);

FT-IR [solid, ν (cm^{-1})]: 2964–2820: [ν(CH) Porph]; 2165: [ν(C≡N) NCO-ligand]; 1093: [ν(–CH_2–O–CH_2–) crypt-222]; 1007: [δ(CCH) Porph].

3. Results and discussion

3.1. Synthesis of complex I

Scheme 1 describes the preparation of H_2TPP, [Cr(TPP)Cl] and [Na(2,2,2-crypt)][Cr^{III}(TPP)$(NCO)_2$]. The first two compounds (a) and (b) were prepared using the method of J. W. Buchler.[27]

3.2. Optical absorption investigation

The electronic spectrum of H_2TPP is described in Fig. 1.

Fig. 2 shows the UV-visible absorption spectra, recorded in chloroform, for the starting compound [Cr^{III}(TPP)Cl] and our derivative [Na(2,2,2-crypt)][Cr^{III}(TPP)$(NCO)_2$]·0.406$CHCl_3$ (**I**). The maximum wavelengths (λ_{max}) of these compounds were compared with those of other arylporphyrins and Cr(III)-arylporphyrin complexes, as shown in Table 2.

The electronic spectrum of the free base H_2TPP shows a strong absorption band, known as the Soret (or B) band, positioned at 419 nm. This band corresponds to a permitted transition from the initial state to the second excited state (S_0 ←

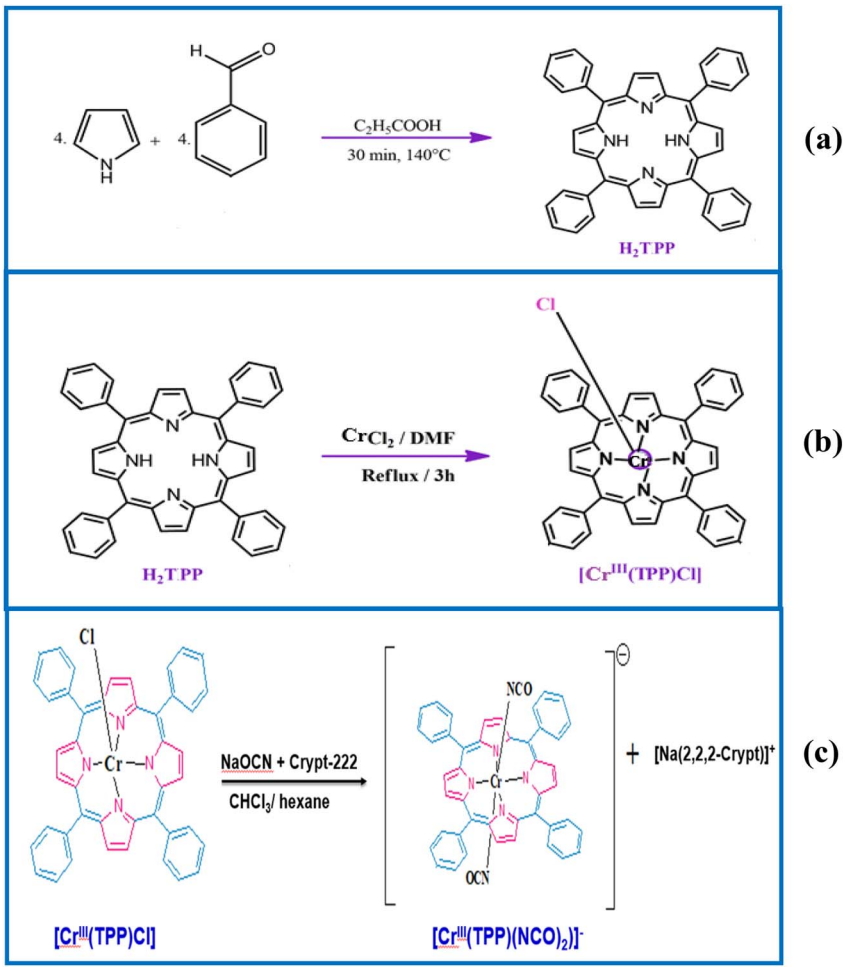

Scheme 1 Synthesis of (a) H_2TPP, (b) [Cr(TPP)Cl] and (c) [Na(2,2,2-crypt)][Cr(TPP)$(NCO)_2$].

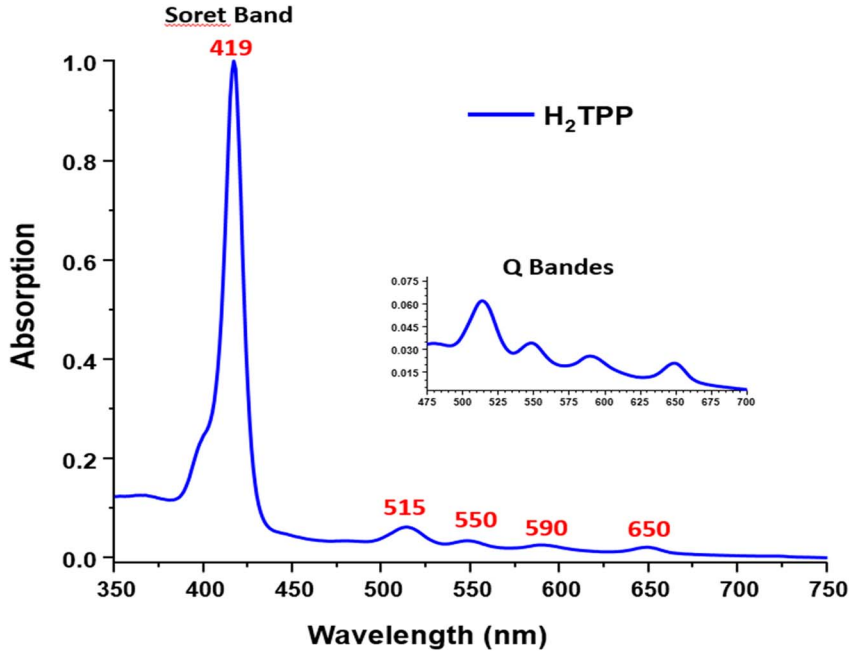

Fig. 1 UV-Vis spectrum of H_2TPP, recorded in $CHCl_3$ at room temperature with a concentration of $\sim 10^{-6}$ M.

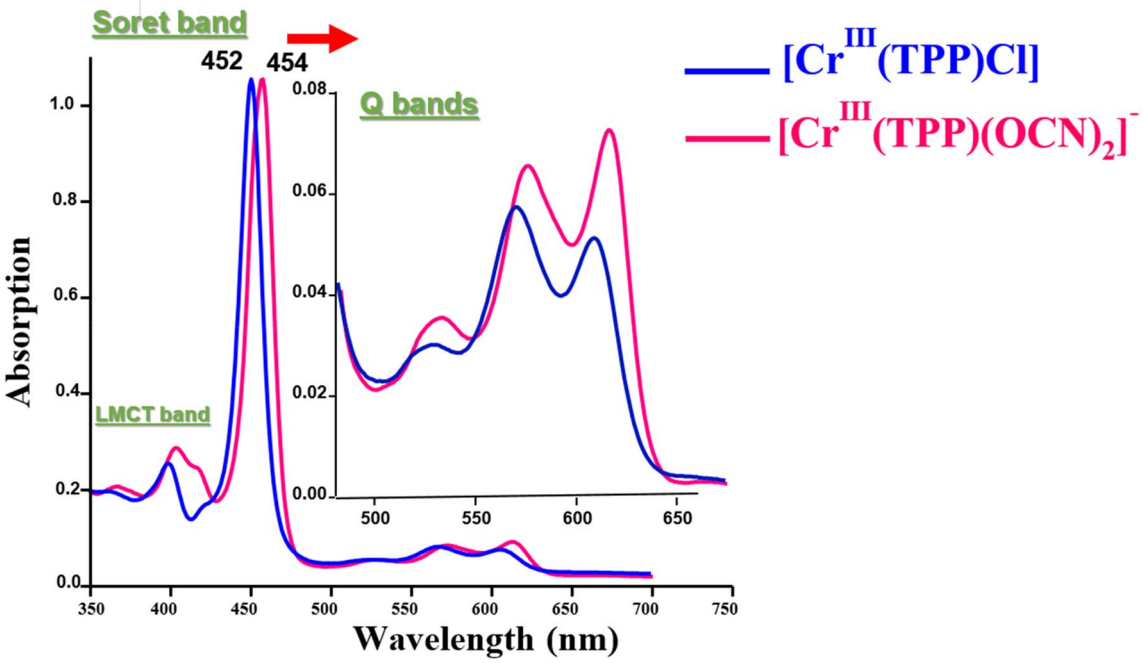

Fig. 2 UV-Vis spectra of $[Cr^{III}(TPP)Cl]$ (blue) and complex **I** (red), recorded in $CHCl_3$ at room temperature with a concentration of $\sim 10^{-6}$ M.

S_2). Additionally, four less intense Q bands are observed at 515, 550, 590, and 650 nm. These are assigned to the Q_y (1, 0), Q_y (0, 0), Q_x (1, 0), and Q_x (0, 0) absorption bands, respectively, and correspond to forbidden transitions from the ground state to the first excited state ($S_0 \leftarrow S_1$).

In the UV-visible study of porphyrin complexes, it is noted that the grouping in the *meta*-substitution of the porphyrin core has no effect. However, the insertion of the metal and the coordination of a ligand have a large effect.[33] This can be explained by an increase in π-conjugation, resulting from the addition of the donor axial ligand.

As shown in Fig. 2, the electronic spectra of $[Cr^{III}(TTP)Cl]$ and complex **I** in a $CHCl_3$ solution exhibit the low-intensity band (LMCT band) in the Soret region, which is slightly red-shifted

compared to that of the chloride chromium(III) derivative. The λ_{max} values of the Soret bands of the chloride and bis(cyanato-*N*) complexes are not the same, and the absorption bands in the Q region are red-shifted. This probably can be explained by the negative charge of this complex.[34] Comparing our synthesized compound with pentacoordinated Cr(III) complexes, we deduced that the Soret band is deflected little towards the red, while it is deflected a lot towards the red compared with the Cr(II) complexes. The shift in the Soret and Q bands in the absorption spectra of $[Cr^{III}(TPP)Cl]$, $[Cr^{III}(TPP)(CN)_2]^-$,[35] and $[Cr^{III}(TPP)(OCN)_2]^-$ has been discussed. This hypsochromic shift was found to be axial ligand dependent, and from the spectrochemical series of ligands, it is concluded that the anionic ligand CN^- is a stronger π-acceptor ligand than NCO^-, leading to the transfer of electrons from the Cr-porphyrins, which may be an effect on the Soret band.

The optical band gap is a key property describing semiconductor physics. The optical band gap energy ($E_{g\text{-opt}}$) values of H_2TPP and $[Cr^{III}(TPP)Cl]$ (see Fig. S1), calculated using the Tauc method,[36,37] are 1.86 and 1.93 eV, respectively. However, in complex **I**, this value is 1.96 eV, which was determined using the tangent method according to the formula:

$$E_{g\text{-opt}} = \frac{1240}{\lambda_{lim}}$$

where λ_{lim} is the intersection between the tangent to the highest Q band and the horizontal (see Fig. S2). These values indicate that the three studied porphyrinic compounds exhibit semiconducting behavior, a common feature of all porphyrins and metalloporphyrins. It is worth noting that the optical gap of the studied complexes remains largely unchanged, although its low value may be advantageous for potential use in the development of new organic semiconductor materials for optoelectronic applications and related compounds.[30]

3.3. IR spectroscopy

The IR spectra of H_2TPP porphyrin and complex **I** are depicted in Fig. 3. The values of some infrared spectroscopic data of $[Na(2,2,2\text{-crypt})][Cr^{III}(TPP)(NCO)_2]$ and other arylporphyrins and Cr(III)-arylporphyrin complexes are reported in Table 3.

H_2TPP exhibits a characteristic IR spectrum of a *meso*-arylporphyrin with ν(NH) and ν(CH) stretching frequencies at 3420 cm^{-1} and in the range of 2930–2829 cm^{-1}, respectively.

The metalation of H_2TPP with chromium(II) chloride dihydrate ($CrCl_2 \cdot 2H_2O$) in THF to form the complex $[Cr^{III}(TPP)Cl]$ leads to the disappearance of the absorption band ν(NH) and the shift toward the high fields of the δ(CCH) bending vibration from 969 cm^{-1} to 1000 cm^{-1}.

For our compound $[Na(2,2,2\text{-crypt})][Cr^{III}(TPP)(NCO)_2]$, there is a strong band in the IR spectrum at 1093 cm^{-1}, which is attributed to the counterion (cryptand-222) sodium(+), and the δ(CCH) bending frequency value is 1007 cm^{-1}. The absorption bands assigned to ν_a(CN) and ν_s(CN) of the cyanate group are 2165 cm^{-1} and 1300 cm^{-1}. The presence of the counterion and $\delta(CCH)_{porph}$ at 1007 cm^{-1} confirmed the presence of hexacoordinate chromium(III) porphyrin species with the bis cyanate axial ligands.

The UV-visible and IR spectroscopies cannot give us a decisive answer or confirm the ground-state electronic configuration of the central-ion.

3.4. Crystal structure of complex I

The crystal was grown by slow diffusion of non-solvent hexane in chloroform. The complex crystallized in the triclinic system (space group *P*1). The asymmetric unit contained two molecules of the $[Na(2,2,2\text{-crypt})][Cr^{III}(TPP)(NCO)_2]$ complex and 0.406 molecules of chloroform solvent.

Table 2 UV-visible spectra of the free base H_2TPP, the precursor $[Cr^{III}(TPP)Cl]$, our derivative $[Na(2,2,2\text{-crypt})][Cr^{III}(TPP)(NCO)_2]\cdot 0.406CHCl_3$ (**I**) and a range of related chromium(III)-porphyrins

	λ_{max} (nm) ($\varepsilon \times 10^{-3}$ M^{-1} cm^{-1})							
Compounds	Soret band		Q bands				$E_{g\text{-opt}}$ (eV)	References
Free *meso*-arylporphyrins in $CHCl_3$								
$[H_2(TPP)]$	**419**(6.08)	515(5.73)	550(4.33)		590(4.20)	650(4.21)	1.86	This work
$[H_2(TMPP)]^a$	**420**(5.95)	518(5.81)	556(4.37)		595(4.24)	653(4.17)	1.87	28
$[H_2(TClPP)]^b$	**417**(5.95)	515(5.82)	553(4.28)		598(4.17)	646(4.10)	1.87	29
$[H_2(TTP)]^c$	**422**(6.11)	519(5.03)	556(4.94)		594(4.84)	651(4.85)	1.86	29
Cr(III) *meso*-arylporphyrin complexes in $CHCl_3$								
$[Cr^{III}(TTP)Cl]$	400(4.44)	**452**(5.15)	525(3.75)		566(3.39)	605(3.90)	1.94	30
$[Cr^{III}(TPP)(NCO)_2]^-$	404(4.24)	**453**(5.14)	532(2.59)		584(3.39)	619(3.71)	1.97	30
$[Cr^{III}(TPP)(OAc)]^d$	396(3.34)	**450**(5.20)	523(3.65)		565(3.99)	605(3.90)	—	31
$[Cr^{III}(TPP)Cl]$	401(4.26)	**452**(5.15)	525(2.75)		556(3.62)	598(3.82)	1.93	This work
$[Cr^{III}(TPP)(NCO)_2]^-$	403(4.25)	**454**(5.13)	534(2.56)		583(3.41)	618(3.72)	1.96	This work
Cr(II) *meso*-arylporphyrin complexes in THF								
$[Cr^{II}(TPP)]$	402	**421**	460	516	601	655	—	32
$[Cr^{II}(TPP)(1\text{-MeIm})_2]^e$	404	**423**	453	532	620	682	—	32

[a] TMPP: *meso*-tetra-methoxyphenylporphyrinato. [b] TClPP: *meso*-tetra-chlorophenylporphyrinato. [c] TTP: *meso*-tetratolylporphyrinato. [d] OAc: Acetato. [e] 1-MeIm: 1-methylimidazole.

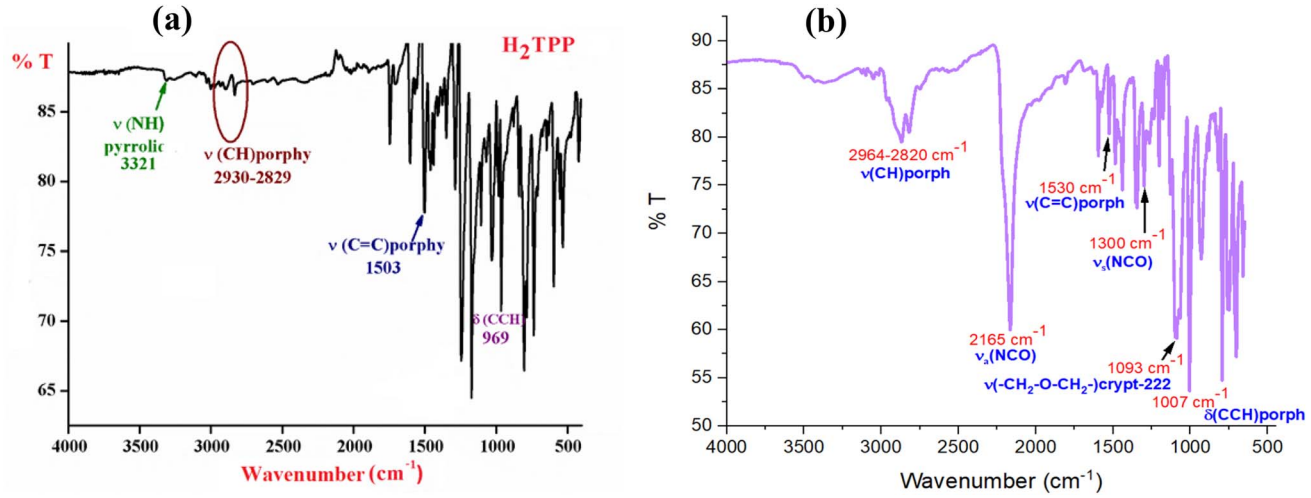

Fig. 3 Experimental IR spectra of (a) H_2TPP and (b) complex **I**.

Table 3 Some IR data of complex **I** and other arylporphyrins and Cr(III)-arylporphyrin complexes[a]

Compound	ν(NH)	ν(CH)	δ(CCH)	ν(CN)L_{ax}[b]	Reference
H_2(TPP)	3321	2930–2829	969	—	This work
H_2(TTP)[c]	3317	3020–2930	952	—	29
H_2(TMPP)[d]	3313	2996–2814	969	—	38
[Cr^{III}(TPP)Cl]	—	3025–2847	1000	—	This work
[Cr^{III}(TTP)Cl]	—	3025–2847	1002	—	30
[Cr^{III}(TMPP)Cl]	—	3059–2849	1001	—	39
[Na(222)][Cr^{III}(TPP)$(NCO)_2$]	—	2973–2819	1007	2165	This work
[K(222)][Cr^{III}(TTP)$(NCO)_2$]	—	2973–2819	1006	2196–2149 (sh)	30
[K(222)][Cr^{III}(TMPP)$(NCS)_2$][e]	—	2957–2810	1005	2050	39

[a] Absorption bands IR (cm^{-1}). [b] L_{ax}: axial ligand. [c] TTP: *meso*-tetratolylporphyrinato. [d] TMPP: *meso*-tetra-methoxyphenylporphyrinato. [e] NCS: thiocyanato.

Fig. 4 depicts an ORTEP diagram[40] of the [Cr^{III}(TPP)$(NCO)_2$]$^-$ ion complex.

The Cr(III) center metal is coordinated to the four nitrogen atoms of the TPP porphyrinato and the bis-cyanate axial ligands with the nitrogen atoms.

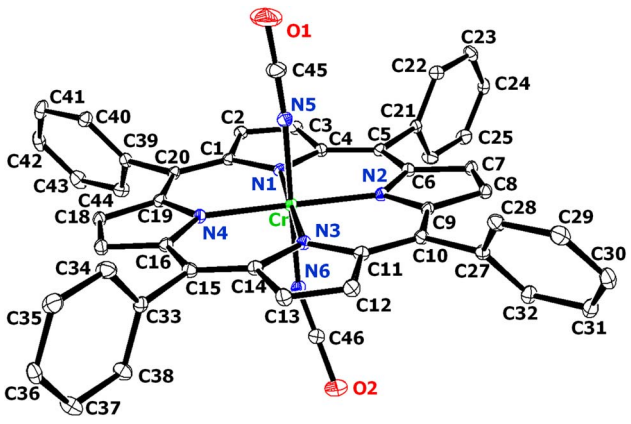

Fig. 4 ORTEP view of the [Cr^{III}(TPP)$(NCO)_2$]$^-$ ion complex; thermal ellipsoids are drawn at the 30% probability level. Hydrogen atoms are omitted for clarity.

Fig. S3 and 5 illustrate the ORTEP diagrams of the [Na(2,2,2-crypt)][Cr^{III}(TPP)$(NCO)_2$]·0.406$CHCl_3$ complex and the [Na(2,2,2-crypt)]$^+$ counterion, respectively (only the major position of the disordered is shown).

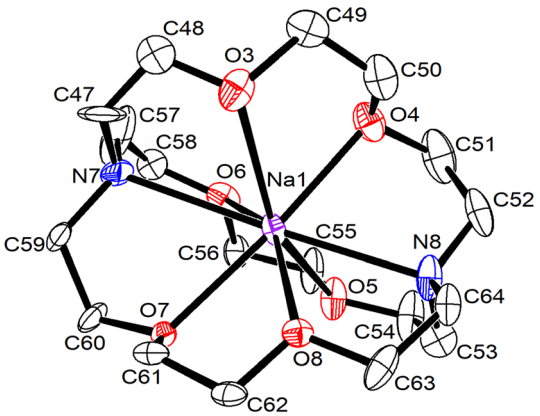

Fig. 5 ORTEP view of [Na(2,2,2-crypt)]$^+$ counterion; the thermal ellipsoids are drawn at the 30% probability level. Only the major position of the disordered is shown. Hydrogen atoms have been omitted for clarity.

Table 4 Selected bond lengths [Å] and angles [°] of [Na(2,2,2-crypt)][Cr^{III}(TPP)$(NCO)_2$] and chromium(III) *meso*-arylporphyrins

Complex	Cr–N_p[a]	Cr–L_{ax}[b]	Reference
[Cr^{III}(TPP)$(NCO)_2$]$^-$	2.039(3)	2.012(3)/2.016(3)	This work
[Cr^{III}(TTP)$(NCO)_2$]$^-$[c]	2.042(4)	2.019(4)/2.019(4)	30
[Cr^{III}(TPP)(N_3)(py)]	2.031(5)	2.004(5) (azido)/2.135(5) (py)	41
[Cr^{III}(TPP)(Cl)(py)]	2.038(8)	2.294(4) (Cl)/2.12(1) (py)	42
[Cr^{III}(TPP)(Cl)(H_2O)]	2.043(2)	2.311(4) (Cl)/2.057(2) (H_2O)	43

[a] Average equatorial distance between the chromium center metal and the nitrogen atoms of the pyrrole rings. [b] Chromium–axial ligand distance. [c] TTP refers to tetratolylporphyrin.

The charge of the anionic complex [Cr^{III}(TTP)$(NCO)_2$]$^-$ is balanced by the counterion [Na(2,2,2-crypt)]$^+$. The sodium atom is eight-coordinated, where it is coordinated to two nitrogen atoms and six oxygen atoms of the cryptand-222. The average Na–O(crypt-222) distance is 2.569(7) Å (K–O (2,2,2-crypt), 2.774 Å[30]), and the average Na–N(crypt-222) bond length is 2.812(8) Å ((K–N (2,2,2-crypt), 3.099 (6) Å)[30]). It is concluded that there is a small difference between both complexes, indicating the good atomic organization and stability of our Na counterion.

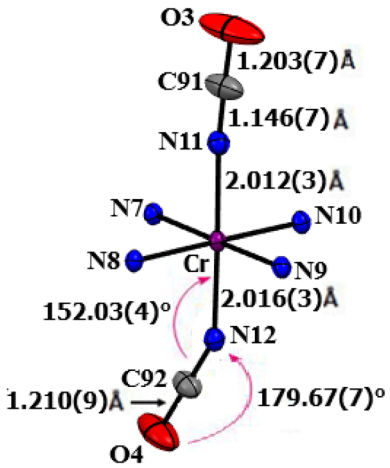

Fig. 6 Coordination polyhedron of Cr^{3+} in the complex ion [Cr^{III}(TTP)$(NCO)_2$]$^-$.

Several bond distances and angles of complex **I**, as well as those of several related Cr(III) *meso*-tetra-arylporphyrins are listed in Table 4.

The bis Cr_2(III)–N(NCO) bond lengths are 2.012(3) and 2.016(3) Å, respectively, which are within the range of the two non-porphyrinic (cyanato-*N*)-chromium(III) complexes reported in the literature: [$Cr^{III}(NCO)_2(L_1)_2$]$^-$ (L_1 = *N*,*N*-bis(3,5-di-*tert*-butylsalicylidene)-1,2-ethylenediamino)[44] and [Cr^{III}(NCO)$(NO)_2$(Cp)] (Cp = cyclopentadienyl)[45] with values of 2.025 and 1.980 Å, respectively.

Fig. 6 represents the coordination polyhedron of the bis-cyanato chromium(III) tetraphenylporphyrin derivative (**I**). Thus, the Cr(III) cation is located at the center of the porphyrin core and defines a distorted square pyramidal environment of four nitrogen atoms of the porphyrin macrocycle and the bis-cyanate axial ligand of two nitrogen atoms.

The bis-axial NCO^- ligand of complex **I** was found to be practically linear with N11–C91–O3 and N12–C92–O4 angles of 178.37(7)° and 179.67(7)°, respectively, as has been observed for all known complexes containing the cyanate-*N* ligand. The value of the Cr2–N11–C91 angle is equal to 174.2(4)° and is within the typical range (137–180°) for various complexes with the cyanato-*N* ligand.

The N11–C91 and C91–O3 distances in the one axial NCO^- ligand are 1.146(7) and 1.203(9) Å, respectively, which are very

Table 5 Bond distances (Å) and angles (deg.) for complex **I** and some porphyrin and non-porphyrin cyanato-*N* complexes

Complexes	M–N(NCO)	N–C	C–O	N–C–O	M–N–C	Reference
Cyanato-*N* metalloporphyrins						
[Cr^{III}(TPP)$(NCO)_2$]$^-$	2.012(3)	1.146(7)	1.203(9)	178.37(7)	174.2(4)	This work
	2.016(3)	1.151(7)	1.210(9)	179.67(7)	152.03(4)	
[Cr^{III}(TTP)$(NCO)_2$]$^-$	2.019(4)	1.148(7)	1.234(9)	174.6(13)	155.2(5)	30
[Mg(TPP)(NCO)]$^-$	2.0471(17)	1.165(2)	1.210(2)	178,34(2)	157.34(15)	46
[Zn(TTP)(NCO)]$^-$[a]	2.0293(3)	1.200(5)	1.163(4)	179.66	137.00(3)	47
[Mn^{III}(TPP)(NCO)]	2.029(5)	1.124(9)	1.200(9)	179.25	150.0(5)	48
[Fe^{II}(TpivPP)(NCO)]$^-$[b]	2.005(3)	1.150(5)	1.200(5)	179.9(5)	176.6(3)	49
[Co^{III}(TPP)$(NCO)_2$]$^-$	1.905	1.151	1.202	178.6	159.8	50
	1.919	1.155	1.193	176.9	144.6	
Non-porphyrinic cyanato-*N* chromium(III) complexes						
[$Cr^{III}(NCO)_2(L_1)_2$]$^-$[c]	2.025	1.173	1.209	177.01	162.08	44
[Cr^{III}(NCO)$(NO)_2$(Cp)][d]	1.980	1.126	1.180	178.59	180	45

[a] TPP = *meso*-tetratolylporphyrinato. [b] TpivPP = α,α,α,α-tetrakis(*o*-pivalamidophenyl)porphyrinate. [c] L_1 = *N*,*N*-bis(3,5-di-*tert*-butylsalicylidene)-1,2-ethylenediamine. [d] Cp = cyclopentadienyl.

close to those of the (cyanato-*N*)–porphyrinic and non-porphyrinic Cr(III) complexes reported in the literature (Table 5). These bond lengths are also similar to those of the NaOCN salt (N–C = 1.16 Å and C–O = 1.27 Å), which probably indicates an ionic character of the Cr2–N(NCO) bond.

Fig. 7 is a formal diagram of the porphyrin macrocycle of $[Cr^{III}(TPP)(NCO)_2]^-$, which shows the displacements of each atom of the $C_{20}N_4Cr$ plane from the 24-atom core plane of the porphyrin in units of 0.01 Å. As shown in this figure, the distance between iron and the 24-atom mean plane of the porphyrin ring (Cr-P_C = 1.08(1) Å) is very small; this explains that the porphyrin ring for $[Cr^{III}(TPP)(NCO)_2]^-$ exhibits a planar conformation.

The content of the unit cell is depicted in Fig. 8, which is made by two $[Cr^{III}(TPP)(NCO)_2]^-$ ion complexes, two [Na(2,2,2-crypt)]$^+$ counterions and 0.406 molecules of chloroform solvent.

The intermolecular interactions within the crystal lattice have been generated using the PLATON program[23] are: classic hydrogen bands such as non-conventional hydrogen bonds such as C–H···O and C–H···Cl interactions.[23,51]

For complex **I**, the intermolecular interactions responsible for the stability of the crystal lattices are of type C–H···O and C–H···Cl.

The visualization of the intermolecular interactions within the crystal lattice of complex **I** was made using the MERCURY program.[24] These intermolecular contacts are depicted in Fig. 9 and 10, while the values of these distances are given in Table S1.

As shown in Fig. 9, the chloride Cl1A of the chloroform solvent is H-bonded to the carbon C88 of one pyrrole ring of a nearby $[Cr^{III}(TTP)(NCO)_2]^-$ ion complex with a C88–H88···CL1A distance of 3.668(5) Å. This Cl1A atom is also linked to the carbon C128 of a close [Na(2,2,2-cryp)]$^+$ counterion with a C128–H12R···Cl1A distance of 3.672(5) Å. Fig. 10 illustrates the C–H···O and C–H···Cl intermolecular interactions. The oxygen O3 of the one axial ligand NCO^- of one $[Cr^{III}(TPP)(NCO)_2]^-$ ion complex and the two carbon atoms C95A and C96A of a neighboring [Na(2,2,2-cryp)]$^+$ counterion are linked by a weak H bond

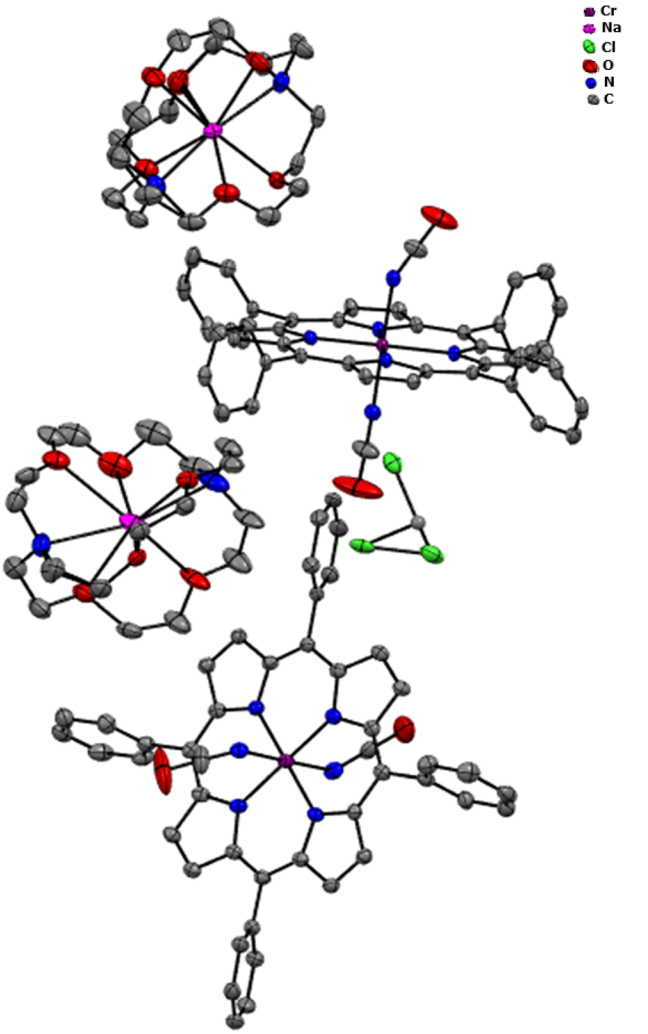

Fig. 8 Cell content of complex I. Only the major positions of the disordered regions are shown. Hydrogen atoms have been omitted for clarity.

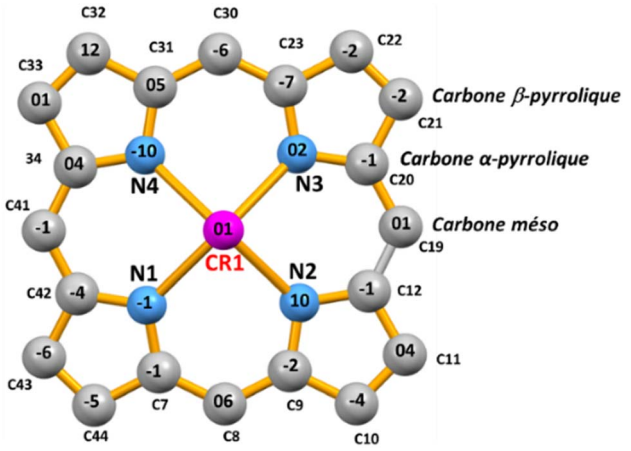

Fig. 7 Formal diagrams of the porphyrin core of $[Cr^{III}(TPP)(NCO)_2]^-$ illustrating the displacement of each atom from the 24-atom core plane in units of 0.01 Å.

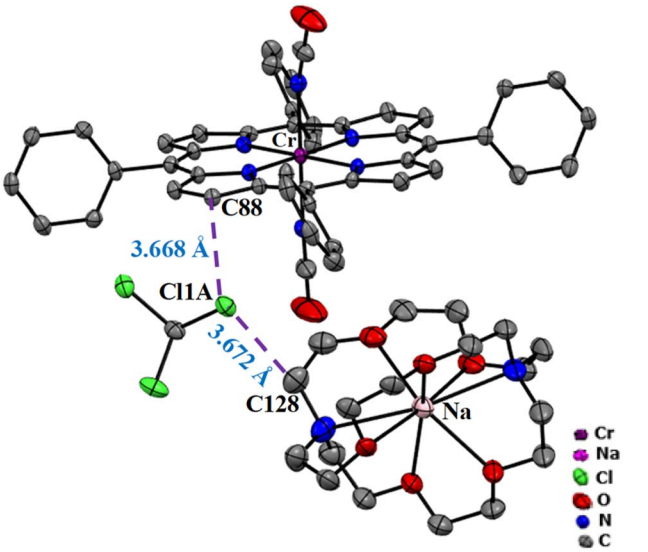

Fig. 9 Drawing illustrating the C–H···Cl intermolecular interactions in the crystal lattice of complex I.

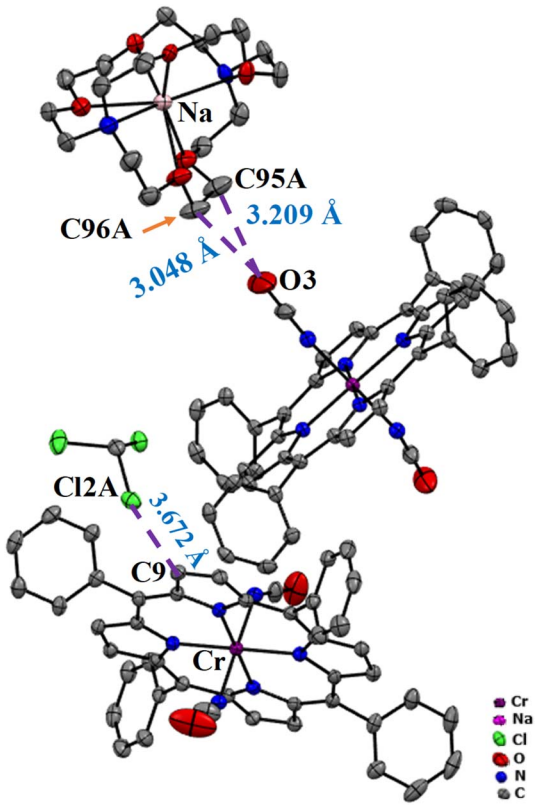

Fig. 10 Drawing illustrating the C–H···O and C–H···Cl intermolecular interactions in the crystal lattice of complex **I**.

with C95A–H95B···O3 and C96A–H96B···O3 distances of 3.209(3) Å and 3.048(3) Å, respectively. The second chloride Cl2A of the chloroform solvent is H bonded to the carbon C9 of one pyrrole ring of a nearby $[Cr(TTP)(NCO)_2]^-$ ion complex with a C9–H9···CL2A distance of 3.714(5) Å.

3.5. Hirshfeld surface analysis

In order to analyze the 3D-Hirshfeld surface (HS) of the chemical compound under consideration, we used in our investigation the well-known software of CrystalExplorer17.5 program.[17,18] However, the d_{norm} normalized contact distance can be estimated by the ratio of van der Waals radii of the atoms and the parameters that describe distances between any surface point to the nearest atom inside and outside the surface given by d_i and d_e, respectively.[17,19] The distance d_{norm} formula is as follows:

$$d_{norm} = \frac{d_i - r_i^{vdW}}{r_i^{vdW}} + \frac{d_e - r_e^{vdW}}{r_e^{vdW}} \quad (1)$$

To make this work more consistent, we have explored the Hirshfeld surface analysis to deeply understand the intermolecular interactions within the complex **I** that are exhibited by X-ray diffraction. Fig. 11 demonstrates the 3D Hirshfeld surfaces mapped with different surfaces for chromium(III) porphyrin complexes.

Firstly, Fig. 11a demonstrates the shape index surface, which describes the topology of the electron density distribution. Generally, it is characterized by these two types of mapping: concave and convex regions depicted in red and blue, respectively, typically indicative of hydrogen bond acceptors and donors. Additionally, the next illustration of Fig. 11b displays the mapped curvedness of our chromium(III) porphyrin complex. It can be observed that there exist several green flat areas separated by blue edges related to high values of curvedness, which contribute to get information about interactions between the closest molecules, which are commonly associated in our case with van der Waals contacts as the white regions in the surface mapped with d_{norm}.

Moreover, in Fig. 11c of d_{norm} is illustrated using a red-to-blue color gradient, ranging from −0.2858 to 1.6287 Å, respectively. The red color visualized with circular depressions or spots in the HS indicates O–H···O, C–H···Cl and C–H···N hydrogen bonds. However, weaker interactions compared to hydrogen bonds are determined with blue- and white-colored regions in HS. As well, the d_{norm} surface is taken as a combination of the d_i and d_e of Fig. 11d and e by eqn (1).

In the same context, we carried out the two-dimensional fingerprint plots for the chromium(III) porphyrin complex in Fig. 12.

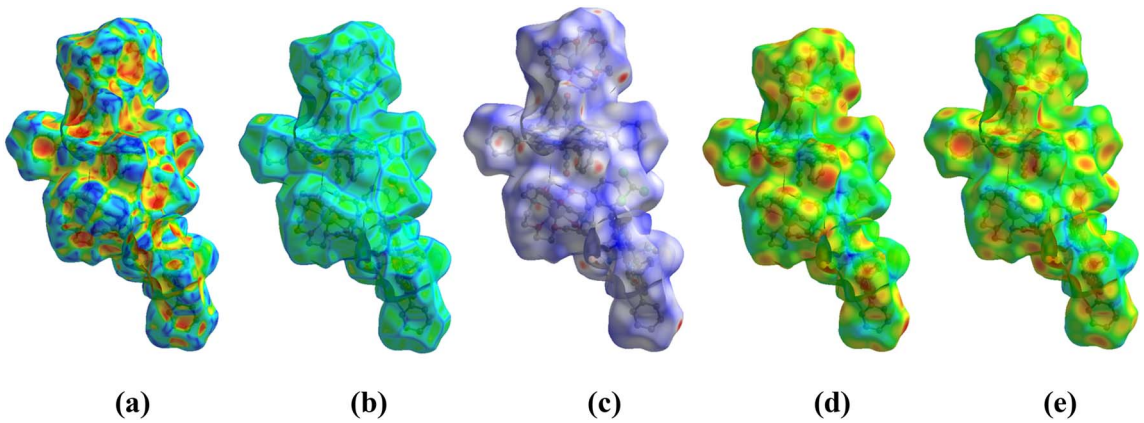

Fig. 11 3D Hirshfeld surfaces mapped with (a) the shape index surface, (b) curvedness surface, (c) d_{norm}, (d) d_i and (e) d_e for chromium(III) porphyrin complexes under consideration.

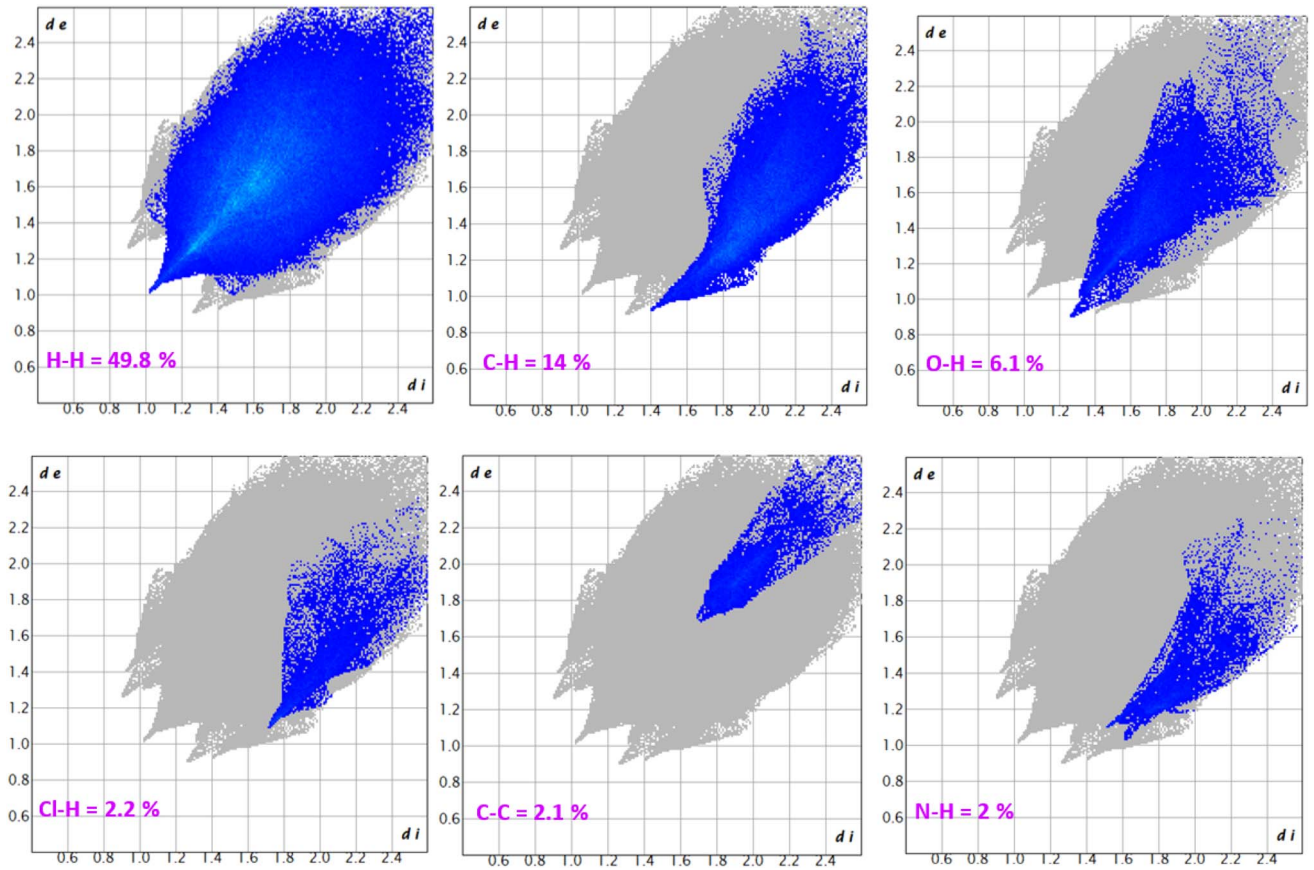

Fig. 12 2D fingerprint plots for chromium(III) porphyrin complexes under study.

Accordingly, the most important contributions of interactions responsible for the structure stability are considered as H···H, C···H/H···C and O···H/H···O contacts for 49.8%, 14% and 6.1%, respectively, of the total HS area. Moreover, the interatomic bonds of Cl···H/H···Cl, C···C and N···H/H···N contribute less than the first ones, with 2.2%, 2.1% and 2% from the total area, respectively.

Commonly, all the 3D Hirshfeld surfaces with the 2D-fingerprint data conform considerably with experimental results, confirming the strong stability and molecular order with atomic arrangement of this synthetized bis(cyanato-*N*)[*meso*-tetraphenylporphyrinato]chromate(III) (cryptand-222) sodium chloroform monosolvate.

3.6. Computational calculations

In order to optimize the molecular structure of synthetized complex **I**, we utilized the functional theoretical level of DFT-D3/B3LYP/LanL2DZ determined in the quantum chemistry software of Gaussian 16.[52] Fig. 13 illustrates the well-optimized structure visualized using GaussView 6.[53]

Obviously, the theoretical values of bond lengths and angles presented in Table 6 are highly close to those extracted from X-ray diffraction analysis data, which display good agreement with the experimental ones, while there is some difference only for angles related to the sodium-cryptand-222, which is due to the difference in matter phase as gas in the theoretical calculation compared to the solid phase in realistic experiment, which confirms that this optimized structure is excellent for deeply understanding more different physical properties of such a substance.

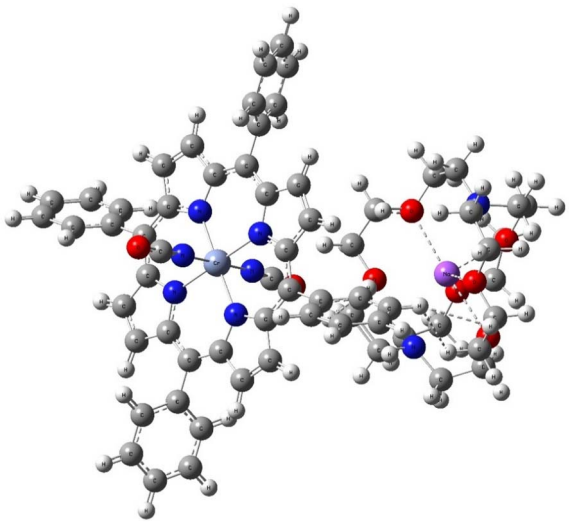

Fig. 13 Optimized structure of complex I under study.

Table 6 Selected experimental and calculated bond distances (Å) and angles (°) of complex I

Distance (Å)	Experimental	Theoretical	Angle (°)	Experimental	Theoretical
Chrome(III) coordination polyhedron of I					
Cr–N4	2.038	2.0529	N4–Cr–N5	90.00	89.1089
Cr–N5	2.032	2.0582	N4–Cr–N7	90.06	91.1891
Cr–N6	2.047	2.064	N4–Cr–N8	91.68	90.6889
Cr–N7	2.056	2.054	N4–Cr–N9	88.94	88.3412
Cr–N8	2.012	1.9161	N5–Cr–N6	89.64	90.706
Cr–N9	2.016	2.0035	N5–Cr–N8	90.03	91.279
			N5–Cr–N9	91.05	89.2877
			N6–Cr–N7	90.30	88.9621
			N6–Cr–N8	88.41	90.1833
			N6–Cr–N9	90.98	90.7883
			N7–Cr–N8	89.71	90.9484
			N7–Cr–N9	89.21	88.4908
Sodium-cryptand-222					
Na84–O86	2.543	2.5269	O86–Na84–O87	102.29	85.8633
Na84–O87	2.614	2.597	O86–Na84–O88	94.56	96.9821
Na84–O88	2.577	2.5109	O86–Na84–O90	92.08	113.2318
Na84–O89	2.698	2.6702	O87–Na84–O88	64.11	66.3752
Na84–O90	2.462	2.8026	O87–Na84–O89	99.33	92.3405
			O87–Na84–O90	114.79	99.1895
			O88–Na84–O89	109.63	87.4619
			O88–Na84–O90	173.34	145.8867
			O89–Na84–O90	63.79	61.4342

3.6.1. Frontier molecular orbitals (FMOs). To better realize integral insights from the electronic structure and the reactivity of the bis(cyanato-*N*)[*meso*-tetraphenylporphyrinato]chromate(III) (cryptand-222) sodium molecular structure, the estimation of frontier molecular orbitals (FMOs) and reactivity descriptors (as well as ionization potential, electron affinity, chemical potential, global hardness and softness, Mulliken Electronegativity and Global Electrophilicity Index) is predicted and illustrated in Fig. 14 and Table 7.

Crucial molecular orbitals that display valuable critical parameters in quantum chemistry are very well known by HOMO and LUMO, representing the highest occupied molecular orbital of the valence band and the lowest unoccupied molecular orbital of the conduction band, respectively.[54] The advantages related to these orbitals lie in the robust estimation of the chemical stability and the electron localization in reactivity sites for further realizing the process of the electronic charge transfer.[55] Moreover, the FMOs contribute greatly to the consideration of the energy separation value between HOMO and LUMO energy levels, known as the gap energy E_g to better understand information about electronic properties with the identification of the competitor groups of donors and acceptors constituting the complex under study, thereby improving its application in different areas as optoelectronic devices and sensor technologies.

According to the results, one may clearly observe that HOMO and LUMO electron densities spread similarly, and their distributions are predominantly localized in the porphyrin ring and the axial ligand around the central anionic chrome(III) ion. It means that donor and acceptor electrons prefer these regions in the structural molecule and the charge transfer can be achieved in such localization between the central ion and its surrounding porphyrin core. As well, our chemical compound exhibited semi-conductor properties as a result of the calculated gap energy, which was found to be approximately 2.136 eV, providing our material suitable application characteristics for next-generation technologies and several electronic devices. The small difference between the theoretical energy gap compared to the experimental one, 1.968 eV, can be attributed to the matter's phase. More precisely, the realistic molecular system is synthesized as a solid material, while the calculated chemical system in the B3LYP/LanL2DZ level of DFT is considered to be more conditioned, as with the gas phase.

According to Table 7, the chemical potential of our complex compound is estimated as a negative value, leading to it being biologically active[56] and having better molecular stability compared to $[K(2,2,2\text{-crypt})][Cr^{III}(TTP)(NCO)_2]\cdot 2H_2O$.[30] In other words, it is difficult to spontaneously disintegrate into separated elements. Also, the global hardness can identify the resistance to different deformations of the electron cloud after chemical treatment of compounds.[57] This Cr(III) complex has a little greater hardness than $[Cr^{III}(TPP)(Cl)(H_2O)]$[43] and $[K(2,2,2\text{-crypt})][Cr^{III}(TTP)(NCO)_2]\cdot 2H_2O$.[30]

3.6.2. Molecular electronic potential (MEP) analysis. The molecular electrostatic potential (MEP) represents a powerful computational approach for elucidating the electronic characteristics of molecular systems, particularly in the identification of reactive sites and the visualization of hydrogen bonding interactions. On the MEP surface map, electron-acceptor (electrophilic) and electron-donor (nucleophilic) regions are typically visualized in red and blue, respectively, corresponding to negative and positive electrostatic potentials. These regions play

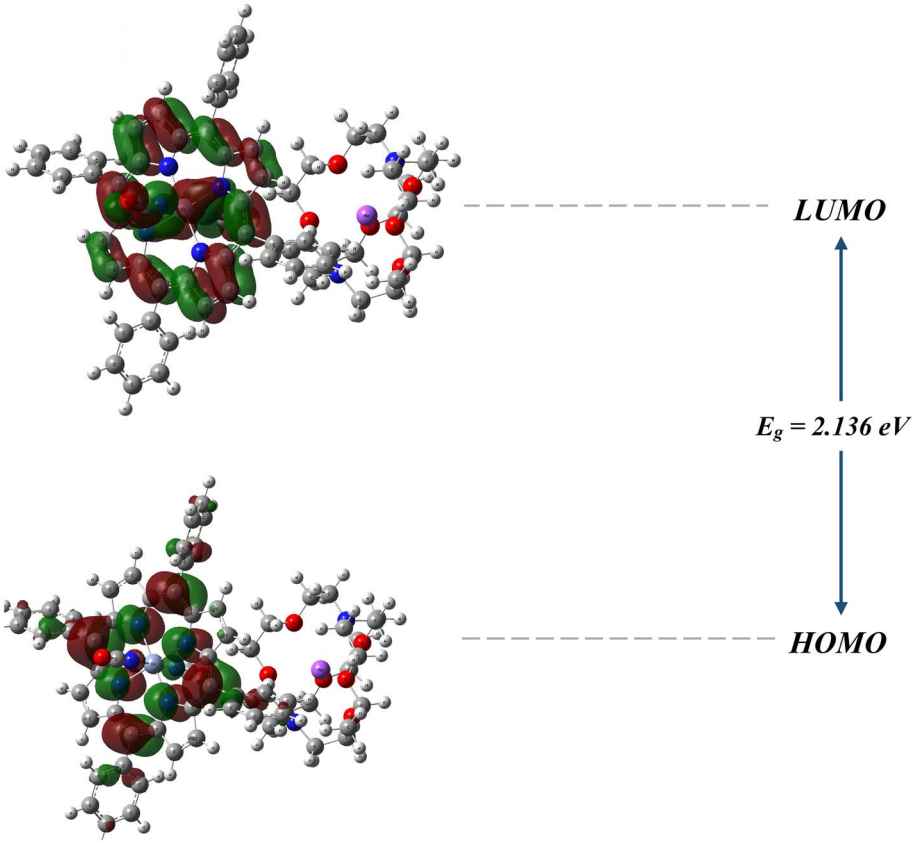

Fig. 14 Three-dimensional visualization of the frontier molecular orbitals for the current complex.

Table 7 Energies of some frontier molecular orbitals and global reactivity parameters computed using the DFT functional of B3LYP/LanL2DZ; all values are expressed in eV, except for S, which is in eV^{-1}

E_{LUMO}	−2.067
E_{HOMO}	−4.203
$E_g = E_{LUMO} - E_{HOMO}$	2.136
Ionization potential ($I \approx -E_{HOMO}$)	4.203
Electron affinity ($A \approx -E_{LUMO}$)	2.067
Chemical potential ($\mu = 1/2\ (E_{LUMO} + E_{HOMO})$)	−3.135
Global hardness ($\eta = 1/2\ (E_{LUMO} - E_{HOMO})$)	1.068
Global softness ($S = 1/2\eta$)	0.468
Mulliken electronegativity ($\chi = -\mu$)	3.135
Global electrophilicity index ($w = \mu^2/2\eta$)	4.601

a crucial role in facilitating electron charge transfer processes within complex systems. Fig. 15 presents the MEP surface of complex **I** from both front and side perspectives.

Notably, the most pronounced electron-accepting regions – colored in red – are located around the chloride axial ligands and the adjacent cationic porphyrin ring, suggesting that these sites possess significant electrophilic reactivity. Conversely, the blue-colored electron-donating region is primarily observed in the cationic species $[Na(2,2,2\text{-crypt})]^+$. The spatial coexistence of these donor and acceptor regions enhances the potential for efficient intramolecular electron charge transfer within the chloride-coordinated complex.

3.6.3. Non-covalent interaction (NCI) and RDG analysis. The well-known theoretical tool of Quantum Theory of Atoms in Molecules (QTAIM), which can provide a description of the inter- and intermolecular interactions for a particular chemical compound, displays a valuable approach in the quantum chemistry calculations. The powerful ability given by such a computation framework is to distinguish and characterize efficiently several interactions depending on different topological parameters such as $H(r)$ (electronic energy density), $G(r)$ (Lagrangian kinetic electron density), $V(r)$ (potential electron density), $\rho(r)$ (electronic charge density), and $\nabla^2\rho(r)$ (its Laplacian at the Bond Critical Point (BCP)). In addition, Johnson *et al.*[58] defined an innovative theoretical method (named NCI-RDG) that provides a model for explaining and identifying the interactions in molecular complexes and small molecules under study, such as hydrogen bonds, van der Waals interactions, and repulsive steric interactions, unlike the experimental interpretations on X-ray diffraction and Hirshfeld surface analysis (HS). NCI analysis is illustrated by a graphical representation defining non-covalent interaction regions, which is efficient to distinguish between interactions (hydrogen bonds, van der Waals and repulsive interactions[59]). While RDG is an effective approach employed in order to analyze non-covalent interactions in real space based on two parameters: electron density and its derivatives.[60] Fig. 16 illustrates the NCI and RDG isosurface of complex **I** under study.

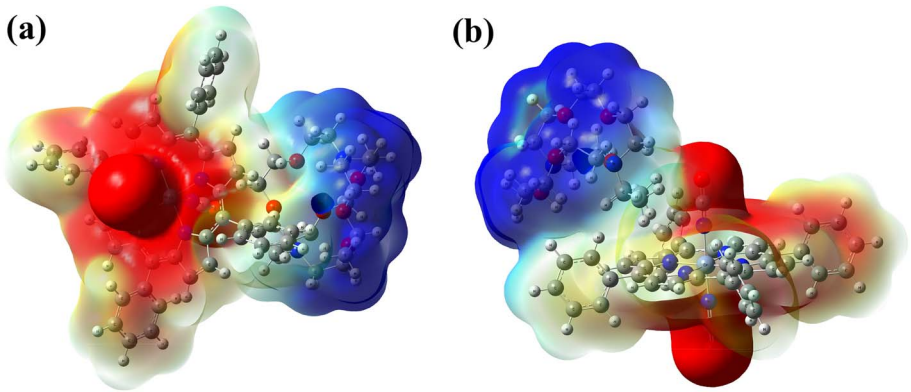

Fig. 15 Molecular electrostatic potential (MEP) surface of complex **I**: (a) front and (b) side views.

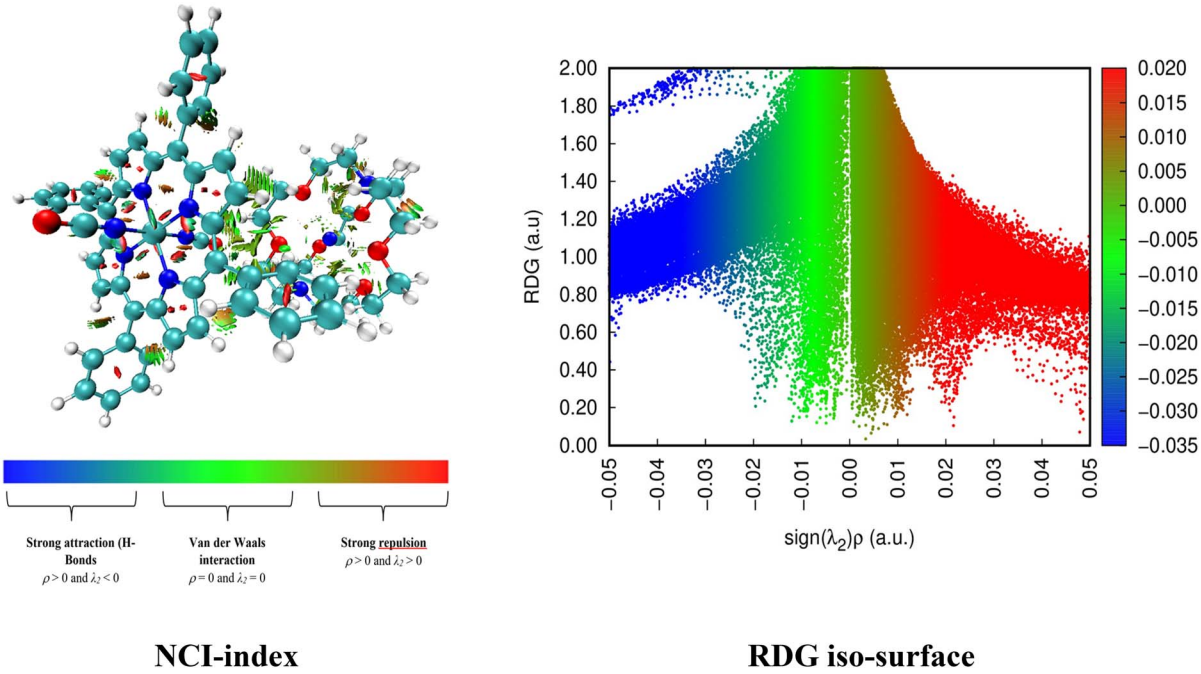

Fig. 16 NCI and RDG iso-surface of complex **I** under study.

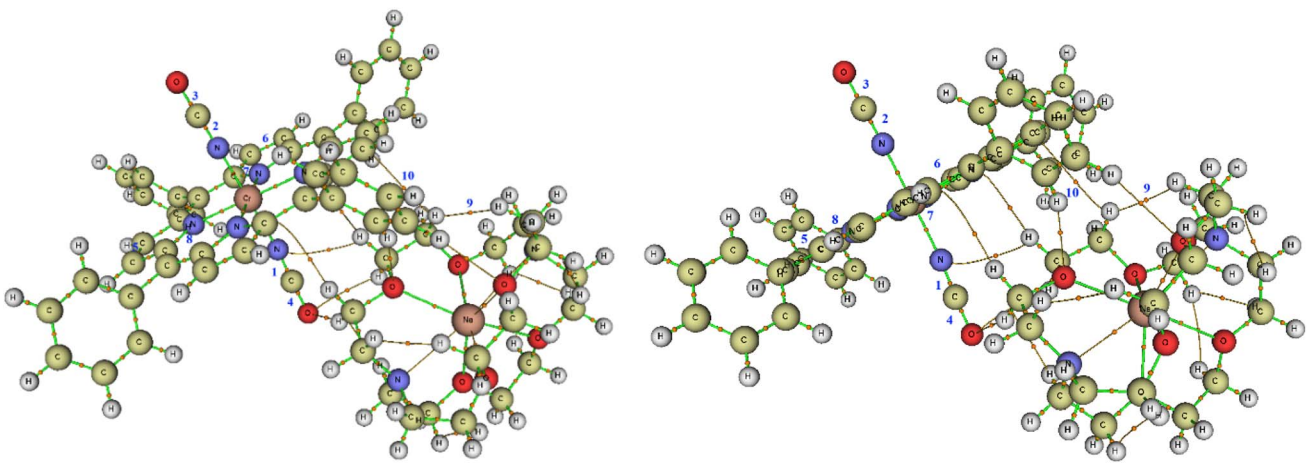

Fig. 17 Different views of the molecular representation of the complex compound with several bond critical points (BCPs).

From these results, the color map in this figure was determined from blue to red, passing through green, related to the strong attraction of hydrogen bonds, strong repulsion of steric effects, and van der Waals interactions. Clearly, the strong repulsions can be seen around the central anionic chromium(III) ion with N atoms in the porphyrin ring. Furthermore, the existences of van der Waals bonds are much depicted in many regions of the chemical compound.

Table 8 Topological parameters calculated at the selected bond critical points (BCPs) (all parameters are expressed in a.u., except for E_{int}, which is in kJ mol^{-1}.)

BCP	$\rho(r)$	$\nabla^2\rho(r)$	$H(r)$	$G(r)$	$V(r)$
1	0.4028	−0.6547	−0.6320	0.4683	−1.1003
2	0.3977	−0.6815	−0.6161	0.4457	−1.0619
3	0.3728	−0.5050	−0.5597	0.4334	−0.9931
4	0.3620	−0.5670	−0.5267	0.3849	−0.9116
5	0.3045	−0.8377	−0.3212	0.1118	−0.4330
6	0.3043	−0.8347	−0.3209	0.1123	−0.4332
7	0.2888	−0.6114	−0.3016	0.1488	−0.4504
8	0.2887	−0.6121	−0.3033	0.1502	−0.4535
9	0.0034	0.0130	0.9712	0.2269	−0.1298
10	0.0033	0.0106	0.7757	0.1896	−0.1120

Besides, the definition of BCP was determined as the point into the bond pathway between two nuclei (or atoms), from which their gradient vector of $\rho(r)$ can be found to be equal to zero ($\nabla\rho(r) = 0$). The bond nature in such BCP is classified by the Laplacian $\nabla^2\rho(r)$. Meanwhile, the bond order defining the strength is relative to the charge density $\rho(r)$. Furthermore, the BCPs of the complex compound are presented in Fig. 17, and their topological parameters are summarized in Table 8.

First, we see that the upper BCP(1) to BCP(4) have the highest $\rho(r)$ values, which are 0.4028, 0.3977, 0.3728, and 0.3620 a.u., respectively. Such bonds represent the strongest interactions in the entire chemical complex **I** related to the chloride axial ligand, between the nitrogen, carbon, and oxygen atoms are bound by N9═C83, N8═C82, C82═O2 and C83═O3. Secondly, the inverse phenomenon is figured straightly in the lower bonds in the table, and the weakest bonds correspond to van der Waals interactions at BCP(9) and BCP(10), which connect the cationic part to the anionic one with H145···H104 and C25···H104, indicating the interaction colored in green in the representation of NCI and RDG iso-surface in Fig. 16.

However, besides the bonds first discussed, the next four bonds (BCP(5) → BCP(8)) relate carbon atoms with carbons and also nitrogen only around the axial ligand in the porphyrin ring.

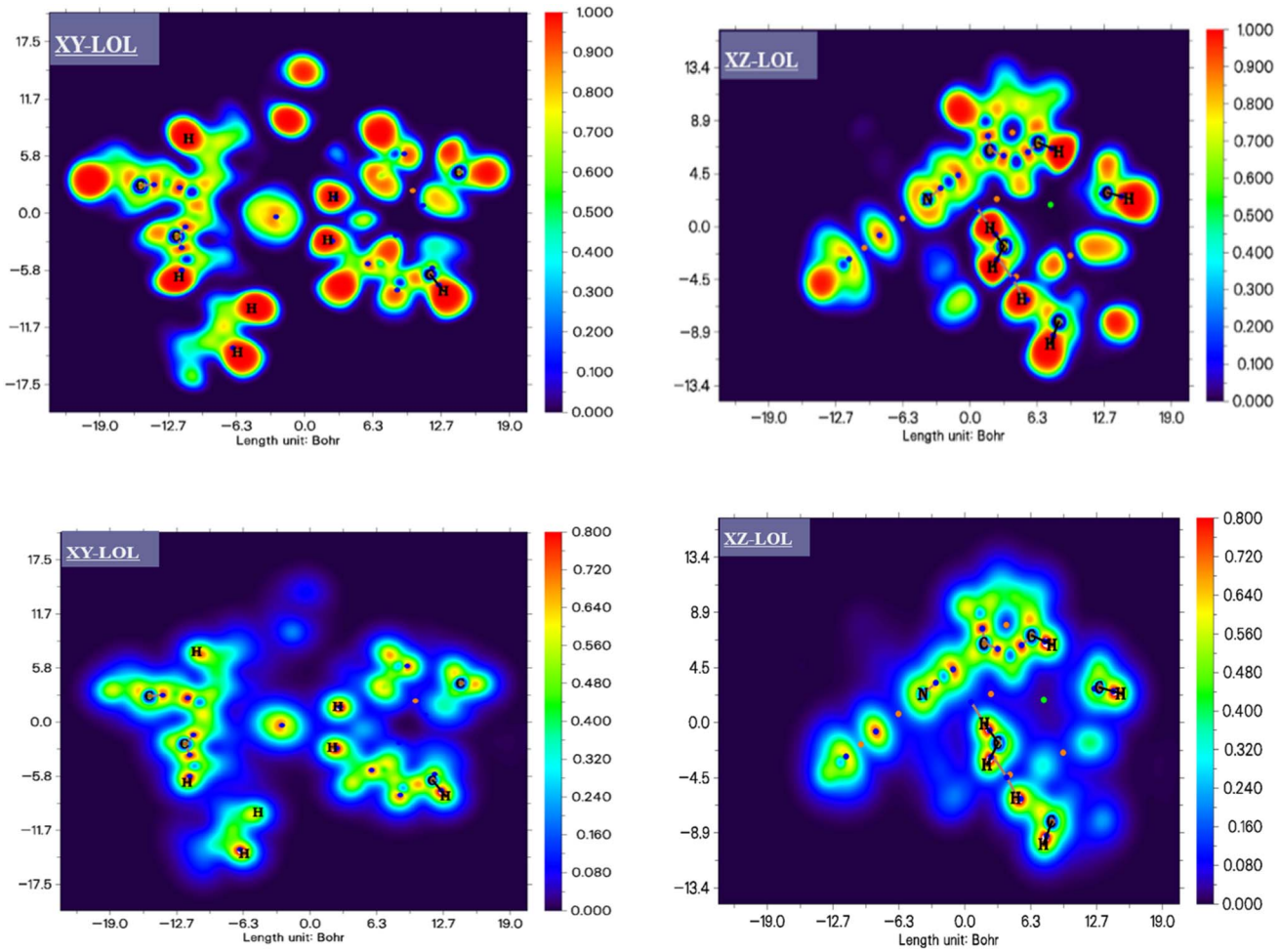

Fig. 18 ELF and LOL iso-surfaces of the studied compound.

Moreover, these findings are confirmed with both of the RDG function iso-surfaces shown in Fig. 16 and the MEP results shown in Fig. 15.

3.6.4. ELF and LOL analyses. The description of chemical structure with topological analysis of the electron localization function (ELF) is published in 1990 by two scientific researchers Silvi and Savin.[61] Commonly, the information provided by such analysis is about the nature of the interactions and the reactivity of the compound under consideration by explaining the density of electron pairs. More precisely, it can be understood from the color scale of the ELF that when its values are approaching 1, Pauli repulsion reaches the maximum and the electrons are perfectly localized in that region. While the inverse observation is attempted when these values are close to 0, Pauli repulsion attains the minimum, and the electrons are completely delocalized in such a region.

Furthermore, the localized orbital locator (LOL) is related to the orbital gradient and presents a prominent descriptor of chemical bonding,[62] providing an explanation of the adapted regions of localized orbitals to maximum overlapping behavior.[63] As qualitative manner, the lowest and highest LOL values characterize the fastest and slowest electrons; such slow particles are associated with localized electrons that could be found in bonds or lone pairs. Both the ELF and LOL iso-surfaces are complementary to each other and display valuable computational methods used in quantum chemistry depending on the kinetic energy density.

The findings of Fig. 18 illustrate the ELF and LOL iso-surfaces of the studied compound with *XY* and *XZ* projections determined using the Multiwfn program.[64]

Clearly, the shaded color maps of the ELF and LOL confirm the strong electronic localization around hydrogen (H) atoms, with a maximum value colored with red indicating the presence of bonding and non-bonding electrons like a covalent bond or a lone pair of electrons in such a region. Meanwhile, the delocalization of the electronic cloud illustrated with blue areas is observed surrounding carbon (C) atoms in the studied compound. Additionally, it should be mentioned that a little white color tint is figured in central regions of some H atoms, which indicates that the electronic density exceeded the maximum color scale limit in such regions. Hence, these differentiations in regions strengthen the electronic charge transfer; otherwise, the more different regions there are in the compound, the better the complex is advantageously stable with the formation of electrostatic interactions between atoms.[65,66] These meaningful conclusions are further supported by MEP and FMO analysis.

4. Conclusion

In summary, we reported the synthesis of the complex [Na(2,2,2-crypt)][Cr^{III}(TPP)$(NCO)_2$]·0.406$CHCl_3$ (complex **I**). This species was characterized by IR and UV-visible spectroscopies and single-crystal X-ray analysis. The bis(cyanato-*N*)-Cr(III) complex crystallized in the non-asymmetric *P*1 space group, and the central metal, chrome, was coordinated by the four nitrogen atoms of the TPP macrocycle and by two nitrogen atoms of the bis-axial cyanate ligand, exhibiting a square-pyramidal geometry with minor distortions. The supramolecular structure of complex **I** was stabilized by intermolecular C–H···Cl and C–H···O interactions, while the π–π stacking of porphyrin rings was not observed. Theoretical predictions and experimental findings exhibited a high degree of concordance, reinforcing the reliability of the computational approach. Moreover, the calculated energy gap highlighted the potential applicability of the studied material in next-generation technologies and a range of electronic devices. The MEP results indicated the spatial co-localization of donor and acceptor regions within the synthesized complex, which underscored its capability for efficient intramolecular electron charge transfer. Furthermore, theoretical analysis of the crystal structure quantified the intermolecular interactions, revealing that crystal packing is predominantly governed by H···H (49.8%), C···H (14%), H···O (6.1%), and H···Cl (2.2%) contacts. Complementary Hirshfeld surface analysis provided additional insights into these interactions, thereby affirming the structural stability and electronic functionality of the complex.

Author contributions

Mondher Dhifet: conceptualization, methodology, writing – original draft, supervision, validation, writing – review & editing. Nabil Benzerroug and Tahani M. Almutairi: conceptualization, writing – review & editing. Khadra B. Alomari, Nikolay Tumanov, and Noureddine Issaoui: conceptualization, methodology, review of the manuscript.

Conflicts of interest

The authors declare that they have no known completing financial interests or personal relationships that could have appeared to influence the work reported in this paper.

Data availability

Data are available from the authors upon request.

CCDC 2414564 contains the supplementary crystallographic data for this paper.[67]

Supplementary information: UV/Vis spectra and X-ray molecular structures are provided in Fig. S1–S3 and Table S1. See DOI: **https://doi.org/10.1039/d5ra04378f**.

Acknowledgements

This work was funded by Researchers Supporting Project number (RSP2025R273), King Saud University, Riyadh, Saudi Arabia.

References

1 O. I. Koifman and T. A. Ageevaa, Main Strategies for the Synthesis of meso-Arylporphyrins, *Russ. J. Org. Chem.*, 2022, **58**, 443–479, DOI: **10.1134/S1070428022040017**.
2 J. R. Charles and R. G. Brian, *Chem. Rev.*, 2004, **104**, 617–649.

3 M. A. F. Elmosallamy, H. A. Hashem and F. F. Abdalmoez, *Anal. Bioanal. Chem.*, 2022, **414**, 8277–8287, DOI: 10.1007/s00216-022-04359-y.
4 N. Rabiee, M. T. Yaraki, S. M. Garakani, S. M. Garakani, S. Ahmadi, A. Lajevardi, M. Bagherzadeh, M. Rabiee, L. Tayebi, M. Tahriri and M. R. Hamblin, *Biomaterials*, 2020, **232**, 119707104, DOI: 10.1016/j.biomaterials.2019.119707.
5 G. Magna, F. Mandoj, M. Stefanelli, G. Pomarico, D. Monti, C. D. Natale, R. Paolesse and S. Nardis, *Nanomaterials*, 2021, **11**, 997, DOI: 10.3390/nano11040997.
6 N. Kobayashi, P. Janda and A. B. P. Lever, *Inorg. Chem.*, 1992, **31**, 5172–5177, DOI: 10.1021/ic00051a006.
7 C.-T. Chen, *Chem. Mater.*, 2004, **16**, 4389–4400, DOI: 10.1021/cm049679m.
8 V. K. Gupta, D. K. Chauhan, V. K. Saini, S. Agarwal, M. M. Antonijevic and H. Lang, *Sensors*, 2003, **3**, 223–235, DOI: 10.3390/s30700223.
9 C. M. Drain, A. Varotto and I. Radivojevic, *Chem. Rev.*, 2009, **109**, 1630–1658, DOI: 10.1021/cr8002483.
10 A. E. O'Connor, W. M. Gallagher and A. T. Byrne, *Photochem. Photobiol.*, 2009, **85**, 1053–1074, DOI: 10.1111/j.1751-1097.2009.00585.x.
11 E. G. Girichev, M. I. Bazanov, N. Z. Mamardashvili and A. Gjeyzak, *Molecules*, 2000, **5**, 767–774, DOI: 10.3390/50600767.
12 R. A. Norwood and J. R. Sounik, *Appl. Phys. Lett.*, 1992, **60**, 295–297, DOI: 10.1063/1.106690.
13 W. A. Nevin and G. A. Chamberlain, *J. Appl. Phys.*, 1991, **69**, 4324–4332, DOI: 10.1063/1.348407.
14 R. Paolesse, S. Nardis, D. Monti, M. Stefanelli and C. Di Natale, *Chem. Rev.*, 2017, **117**, 2517–2583, DOI: 10.1021/acs.chemrev.6b00361.
15 I. Bouamaied, T. Coskun, E. Stulz, (2006) 1–47, DOI: 10.1007/430_021.
16 D. D. Perrin and W. L. F. Armarego, *Purification of Organic Solvents*, Pergamon Press, Oxford, 1988.
17 M. A. Spackman and D. Jayatilaka, Hirshfeld surface analysis, *CrystEngComm*, 2009, **11**, 19–32, DOI: 10.1039/B818330A.
18 S. K. Wolff, D. J. Grimwood, J. J. McKinnon, M. J. Turner, D. Jayatilaka and M. A. Spack-man, *CrystalExplorer 3.1*, University of Western Australia, Crawley, Western Australia, 2013, http://hirshfeldsurface.net/CrystalExplorer.
19 M. A. Spackman and J. J. McKinnon, *CrystEngComm*, 2002, **4**, 378–392, DOI: 10.1039/B203191B.
20 P. McArdle, SORTX-a program for on-screen stick-model editing and autosort- ing of SHELX files for use on a PC, *J. Appl. Crystallogr.*, 1995, **28**, 65, DOI: 10.1107/S0021889894010642.
21 A. Altomare, G. Cascarano, C. Giacovazzo, A. Guagliardi, M. C. Burla, G. Polidori and M. Camalli, *J. Appl. Crystallogr.*, 1994, **27**, 435–436, DOI: 10.1107/S0021889894000221.
22 G. M. Sheldrick, Crystal structure refinement with SHELXL, *Acta Crystallogr., Sect. C: Cryst. Struct. Commun.*, 2015, **71**, 3–8, DOI: 10.1107/S2053229614024218.
23 A. L. Spek, PLATON SQUEEZE: a tool for the calculation of the disordered solvent contribution to the calculated structure factors, *Acta Crystallogr., Sect. C:Struct. Chem.*, 2015, **71**, 9–18, DOI: 10.1107/S2053229614024929.
24 O. Sarkar, M. Roy, N. R. Pramanik, P. Dey, S. K. Seth, M. G. B. Drew and S. Chakrabarti, *J. Mol. Struct.*, 2024, **1301**, 137125, DOI: 10.1016/j.molstruc.2023.137125.
25 T. Fradi, O. Noureddine, F. Ben Taheur, M. Guergueb, S. Nasri, N. Amiri, A. Almahri, T. Roisnel, V. Guerineau, N. Issoui and H. Nasri, *J. Mol. Struct.*, 2021, **1236**, 130299, DOI: 10.1016/j.molstruc.2021.130299.
26 D. A. Summerville, R. D. Jones, B. M. Hoffman and F. Basolo, *J. Am. Chem. Soc.*, 1977, **99**, 8195–8202, DOI: 10.1021/ja00467a012.
27 J. W. Buchler, in *The Porphyrins*, ed. D. Dolphin, Academic Press, New-York, 1978, pp. 390–474.
28 M. Guergueb, S. Nasri, J. Brahmi, F. Loiseau, F. Molton, T. Roisnel, V. Guerineau, I. Turowska-Tyrk, K. Aouadi and H. Nasri, *RSC Adv.*, 2020, **10**, 6900–6918.
29 S. Nasri, M. Guergueb, J. Brahmi, Y. O. Al-Ghamdi, F. Molton, F. L oiseau, I. Turowska-Tyrk and H. Nasri, *Molecules*, 2022, **27**, 8866.
30 A. Kechiche, T. Fradi, O. Noureddine, M. Guergueb, F. Loiseau, V. Guerineau, N. Issoui, A. Lemeune and H. Nasri, *J. Mol. Struct.*, 2022, **1250**, 131801, DOI: 10.1016/j.molstruc.2021.131801.
31 S. V. Zaitseva, S. A. Zdanovich and O. A. Golubchikov, *Russ. J. Coord. Chem.*, 2002, **28**, 843–847, DOI: 10.1023/A:1021630228084.
32 C. A. Reed, J. K. Kouba, C. J. Grimes and S. K. Cheung, *Inorg. Chem.*, 1978, **17**, 2666–2670, DOI: 10.1021/ic50187a057.
33 M. Gouterman, *J. Chem. Phys.*, 1959, **30**, 1139–1161, DOI: 10.1063/1.1730148.
34 H. Nasri, M. K. Ellison, M. Shang, C. E. Schulz and W. R. Scheidt, *Inorg. Chem.*, 2004, **43**, 2932–2942, DOI: 10.1021/ic035119y.
35 A. kechich, R. Soury, M. Jabli, K. M. Alenezi, C. Philouze and H. Nasri, *Inorg. Chem. Commun.*, 2021, **128**, 108588, DOI: 10.1016/j.inoche.2021.108588.
36 J. Tauc, R. Grigorovici and A. Vancu, *Phys. Status Solidi*, 1966, **15**, 627–637.
37 O. Polat, M. Caglar, F. M. Coskun, M. Coskun, Y. Caglar and A. Turut, *Vacuum*, 2020, **173**, 109124.
38 M. Dhifet, H. Mohamed, N. Benzerroug, H. Ghalla, G. Rigane and R. Salem, *Struct. Chem.*, 2025, DOI: 10.1007/s11224-025-02526-2.
39 A. Kechiche, PhD thesis, University of Monastir, Monastir, Tunisia, 2023.
40 L. J. Farrugia, A Version of It ORTEP-III with a Graphical User Interface (GUI), *J. Appl. Crystallogr.*, 1997, **30**, 565, DOI: 10.1107/S0021889897003117.
41 H. Shuo, S. Gu, Y. Liu, R. Jin and H. Yingyong, *J. Appl. Chem.*, 1991, **3**, 67–70.
42 A. L. Balch, L. Latos-Grazynski, B. C. Noll, M. M. Olmstead and E. P. Zovinka, *Inorg. Chem.*, 1992, **13**, 1148–1151.
43 M. Inamo, H. Nakaba, K. Nakajima and M. Hoshino, *Inorg. Chem.*, 2000, **39**(20), 4417–4423.

44 D. J. Darensbourg and A. I. Moncada, *Inorg. Chem.*, 2008, **47**, 10000–10008.
45 M. A. Bush and G. A. Sim, *J. Chem. Soc. A*, 1970, 605–611, DOI: 10.1039/J19700000605.
46 K. Ezzayani, Z. Denden, S. Najmudin, C. Bonifácio, E. Saint-Aman, F. Loiseau and H. Nasri, *Eur. J. Inorg. Chem.*, 2014, 5348–5361.
47 Z. Denden, K. Ezzayani, E. Saint-Aman, F. Loiseau, S. Najmudin, C. Bonifácio, J.-C. Daran and H. Nasri, *Eur. J. Inorg. Chem.*, 2015, 2596–2610.
48 P. Turner, M. J. Gunter, B. W. Skelton and A. H. White, *Aust. J. Chem.*, 1998, **51**, 835–852.
49 M. Dhifet, M. S. Belkhiria, J.-C. Daran, C. E. Schulz and H. Nasri, *Inorg. Chim. Acta*, 2010, **363**, 3208–3213.
50 B. B. Ali, M. S. Belkhiria, J.-C. Daran and H. Nasri, *Acta Crystallogr.*, 2012, **68**, 1262.
51 P. Dey, A. Hossain and S. K. Seth, *J. Mol. Struct.*, 2024, **1295**, 136642, DOI: 10.1016/j.molstruc.2023.136642.
52 M. J. Frisch, G. W. Trucks, H. B. Schlegel, G. E. Scuseria, Ma. Robb, J. R. Cheeseman, G. Scalmani, V. Barone, G. A. Petersson and H. Nakatsuji, *Gaussian 16, Revision A.03*, Gaussian, Inc., Wallingford CT, 2016, vol. 3.
53 D. D. Roy, A. K. Todd and M. M. John, *Gauss View 5.0.8*, Wallingford, Gaussian Inc, 2009.
54 A. S. Kazachenko, F. Akman, A. Sagaama, N. Issaoui, N. Y. Malyar, N. Y. Vasilieva and V. S. Borovkov, Theoretical and experimental study of guar gum sulfation, *J. Mol. Model.*, 2021, **27**, 5.
55 M. DjeribiI. Nagazi, N. Dege, N. Issaoui and, A. Haddad, *Supramolecular architecture of a novel non-centrosymmetric heteromolybdate hybrid for nonlinear optical applications: structure, characterization, stability study and DFT calculations*, Research Square, preprint, 2023, DOI: 10.21203/rs.3.rs-2996132/v1.
56 M. Salihovic, S. Huseinovic, S. Spirtovic-Halilovic, A. Osmanovic, A. Dedic, Z. Asimovic and D. Zavrsnik, *Bull. Chem. Technol. Bosnia Herzegovina*, 2014, **42**, 31–36.
57 M. A. Lutoshkin, A. I. Petrov, B. N. Kuznetsov and A. S. Kazachenko, Aqueous Complexation of Morin and Its Sulfonate Derivative with Lanthanum(III) and Trivalent Lanthanides, *J. Solution Chem.*, 2019, **48**, 676–688.
58 E. R. Johnson, S. Keinan, P. Mori-Sánchez, J. Contreras-García, A. J. Cohen and W. Yang, Revealing Noncovalent Interactions, *J. Am. Chem. Soc.*, 2010, **132**, 6498–6506, DOI: 10.1021/ja100936w.
59 G. Saleh, C. Gatti, L. Lo Presti and J. Contreras-Garcia, Revealing non-covalent interactions in molecular crystals through their experimental electron densities, *Chemistry*, 2012, **18**, 15523–15536.
60 B. Silvi and A. Savin, *Nature*, 1994, **371**, 683–686, DOI: 10.1038/371683a0.
61 K. Arulaabaranam, G. Mani and S. Muthu, Computational assessment on wave function (ELF, LOL) analysis, molecular confirmation and molecular docking explores on 2-(5-Amino-2- Methylanilino)-4-(3-pyridyl) pyrimidine, *Chem. Data Collect.*, 2020, **29**, 100525.
62 C. D. Vincy, J. D. D. Tarika, X. D. D. Dexlin, A. Rathika and T. J. Beaula, Exploring the antibacterial activity of 1, 2 diaminoethane hexanedionic acid by spectroscopic, electronic, ELF, LOL, RDG analysis and molecular docking studies using DFT method, *J. Mol. Struct.*, 2022, **1247**, 131388.
63 J. J. P. Stewart, An examination of the nature of localized molecular orbitals and their value in understanding various phenomena that occur in organic chemistry, *J. Mol. Model.*, 2018, **25**, 7.
64 T. Lu and F. Chen, Multiwfn: A multifunctional wavefunction analyzer, *J. Comput. Chem.*, 2012, **33**, 580–592.
65 I. Chérif, D. Bouazzi, M. T. Caccamo, B. Gassoumi, S. Magazù, B. Badraoui and S. Ayachi, Quantum computational investigation into optoelectronic and topological properties of a synthesized nanocomposite containing Hydroxyapatite-alt-Polyethylene Glycol (HAP/PEG), *Colloids Surf., A*, 2024, **686**, 133442, DOI: 10.1016/j.colsurfa.2024.133442.
66 C. H. Belgacem, N. Missaoui, M. A. H. Khalafalla, G. Bouzid, H. Kahri, A. H. Bashal, A. Dhahri, L. Nouar, F. J. Melendez, M. E. Castro, H. Ghalla and Y. Zhou, Synthesis of ultramicroporous zeolitic imidazolate framework ZIF-8 via solid state method using a minimum amount of deionized water for high greenhouse gas adsorption: A computational modeling, *J. Environ. Chem. Eng.*, 2024, **12**, 112086, DOI: 10.1016/j.jece.2024.112086.
67 M. Dhifet, N. Benzerroug, T. M. Almutairi, K. B. Alomari, N. Tumanov and N. Issaoui, CCDC 2414564: Experimental Crystal Structure Determination, 2025, DOI: 10.5517/ccdc.csd.cc2m1k5f.